GEOPHYSICS, VOL. 82, NO. 4 (JULY-AUGUST 2017); P. WA1–WA10, 10 FIGS., 4 TABLES.
10.1190/GEO2016-0635.1

Numerical simulation of seismic wave propagation in viscoelastic-anisotropic media using frequency-independent *Q* wave equation

Tieyuan Zhu[1]

ABSTRACT

Seismic anisotropy is the fundamental phenomenon of wave propagation in the earth's interior. Numerical modeling of wave behavior is critical for exploration and global seismology studies. The full elastic (anisotropy) wave equation is often used to model the complexity of velocity anisotropy, but it ignores attenuation anisotropy. I have presented a time-domain displacement-stress formulation of the anisotropic-viscoelastic wave equation, which holds for arbitrarily anisotropic velocity and attenuation $1/Q$. The frequency-independent Q model is considered in the seismic frequency band; thus, anisotropic attenuation is mathematically expressed by way of fractional time derivatives, which are solved using the truncated Grünwald-Letnikov approximation. I evaluate the accuracy of numerical solutions in a homogeneous transversely isotropic (TI) medium by comparing with theoretical Q_P and Q_S values calculated from the Christoffel equation. Numerical modeling results show that the anisotropic attenuation is angle dependent and significantly different from the isotropic attenuation. In synthetic examples, I have proved its generality and feasibility by modeling wave propagation in a 2D TI inhomogeneous medium and a 3D orthorhombic inhomogeneous medium.

INTRODUCTION

Velocity anisotropy of seismic wave propagation in the earth's interior, from the shallow crust to the deep mantle and core, has been extensively studied and well-documented in theoretical and exploration seismology (Anderson, 1989; Helbig, 1994; Tsvankin, 2012; Thomsen, 2014). Velocity anisotropy is found to be related to material microstructure, composition or mineralogy, temperature, pressure, and fracture properties. Meanwhile, seismic attenuation is also directionally (angle) dependent, as reported in laboratory studies from ultrasonic measurements in rock samples, including shale, sandstone, limestone, and mudstone (e.g., Tao and King, 1990; Arts and Rasolofosaon, 1992; Domnesteanu et al., 2002; Shi and Deng, 2005; Best et al., 2007; Zhubayev et al., 2016) and composite samples with aligned cracks (e.g., Hosten et al., 1987; Zhu et al., 2007a; Chichinina et al., 2009). Most of these results support the argument that the P-wave attenuation anisotropy is substantially stronger than the velocity anisotropy (e.g., Chichinina et al., 2009; Zhubayev et al., 2016). Attenuation anisotropy was also observed in real seismic data (Liu et al., 1993; Lynn et al., 1999) in which azimuth attenuation is attributed to the preferential alignment of fractures. In theory, Carcione (1992) and Zhu et al. (2007b) find that attenuation anisotropy could also be the result of interbedding thin layers with different velocities and attenuation coefficients even if they are isotropic.

Modeling wave propagation in anisotropic media is the key element of seismic imaging and full-waveform inversion of anisotropic parameters. Considering only velocity anisotropy, wave propagation is well-modeled by the anisotropic elastic-wave equation. In the past few decades, this has been extensively studied, e.g., the most simple transverse isotropy (Thomsen, 1986), practical acoustic anisotropy (Alkhalifah, 2000), and general anisotropy (Komatitsch and Tromp, 1999). However, much less attention has been paid on the study of the wave equation by numerical modeling of directionally dependent attenuation.

Theoretically, Hooke's law for viscoelastic media is expressed in terms of the complex and frequency-dependent stiffness. The anisotropic Q_{ij} constants, by definition (e.g., Carcione, 2014), are C^r_{ij}/C^i_{ij}, where C^r_{ij} are the real parts of the elastic stiffness coefficients, and C^i_{ij} are the imaginary parts of the elastic stiffness coefficients. Frequency-dependent attenuation is represented in the form of the convolution integral in the time domain. The simplest frequency-attenuation dependence is linear, i.e., frequency independent Q (or constant Q), which has been widely used for seismic modeling and inverse problems. Oftentimes, a set of standard linear

Manuscript received by the Editor 30 November 2016; revised manuscript received 5 March 2017; published online 21 April 2017.
[1]The Pennsylvania State University, Department of Geosciences and Institute of Natural Gas Research, University Park, Pennsylvania, USA. E-mail: tyzhu@psu.edu.

solid elements (or Maxwell bodies) with isotropic constitutive equations was used to describe nearly constant-Q anelastic behavior (Liu et al., 1976). Based on Backus averaging, Carcione (1992) numerically studies the effective anisotropic attenuation in viscoelastic-isotropic finely layered media. Komatitsch and Tromp (1999) generalize the isotropic relaxation function to be anisotropic. Bai and Tsvankin (2016) adopt anisotropic relaxation times τ_{ij} in the generalized standard linear solid model and implement a 2D time-domain finite-difference (FD) modeling of vertical transversely isotropic (VTI) attenuation. Because all components Q_{ij} of the quality-factor $\mathbf{Q}$ matrix are desired to be constant within a specified frequency band, the corresponding system of wave equations should be complemented by a set of anisotropic viscoelastic wave equations. The number of (velocity stress) equations is dependent on the number of memory variables, e.g., $5 + 3L$ equations in 2D space and $9 + 6L$ equations in 3D space (Zhu et al., 2013).

In fact, a constant-Q model proposed by Kjartansson (1979) enables to perfectly describe the frequency-independent Q anelastic behavior using less parameters (only Q at the reference frequency ω_0). This model has already been implemented to represent the attenuation behavior in viscoacoustic wave equations (Carcione et al., 2002; Zhu and Harris, 2014) and viscoelastic wave equations (Carcione, 2009; Zhu and Carcione, 2014). The number of equations to be solved is the same as acoustic and elastic equations. Note that all these wave equations were derived for isotropic media.

In this study, I extend an isotropic formulation to a general anisotropic-viscoelastic wave equation that enables to model anisotropic attenuation. In terms of the relaxation function of the constant-Q model, the convolution can be replaced by the fractional time derivatives in the constitutive equation (Carcione et al., 2002; Carcione, 2009). The derived time-domain displacement-stress formulation of the anisotropic-viscoelastic wave equation holds for an arbitrarily anisotropic velocity and attenuation. I investigate the accuracy of the proposed wave equation by comparing it with theoretical solutions for a 2D homogeneous TI model. Finally, I show the results of numerical modeling for 2D TI and 3D orthorhombic media.

THEORY

In this section, I first review the constitutive equation for isotropic viscoacoustic media based on the constant-Q model (Kjartansson, 1979), and then I generalize the derivation of the constitutive equation by incorporating anisotropic attenuation. Following this, I explain a numerical scheme, i.e., a truncated Grünwald-Letnikov (GL) approximation, to solve fractional time derivatives. Finally, I summarize the main steps of the FD method to solve the 2D TI viscoelastic wave equations.

Constitutive equations

Considering the constant-Q model (Kjartansson, 1979), the relaxation function is defined as

$$\psi(t) = \frac{M_0}{\Gamma(1-t)}\left(\frac{t}{t_0}\right)^{-2\gamma} H(t), \tag{1}$$

where M_0 is a bulk modulus; Γ is Euler's gamma function; $t_0 = 1/\omega_0$, where ω_0 is a reference frequency; γ is a dimensionless parameter $\gamma = \arctan(1/Q)/\pi$, which yields to the fractional power γ with the range of [0, 0.5]; and H is the Heaviside step function. Therefore, in isotropic viscoacoustic media, the constitutive equation in terms of a fractional derivative (Carcione et al., 2002) is given as

$$\sigma(\mathbf{x}, t) = M_0 \omega_0^{-2\gamma} \partial_t^{2\gamma} \varepsilon(\mathbf{x}, t). \tag{2}$$

Unlike the idea of a fractional Laplacian operator with some degree of approximation (Zhu and Harris, 2014), this fractional time derivative operator is used without any approximation.

The generalized time-domain constitutive equation for the anisotropic-viscoelastic medium (Carcione, 2014) is expressed as

$$\sigma_{ij}(\mathbf{x}, t) = \psi_{ijkl}(\mathbf{x}, t) * \partial_t \varepsilon_{kl}(\mathbf{x}, t), \tag{3}$$

where t is the time variable, $\mathbf{x}$ is the position vector, $*$ denotes the time convolution, σ_{ij} are the components of the stress tensor, ψ_{kl} are the components of the strain tensor, $\psi_{ijkl}(\mathbf{x}, t)$ are the components of the relaxation function stiffness tensor of the medium properties, and $i, j, k, l = 1, 2, 3$.

Analogous to the anisotropic Zener model (Komatitsch and Tromp, 1999), from equation 1, the anisotropic relaxation function of the frequency-independent Q model can be defined as

$$\psi_{ijkl}(\mathbf{x}, t) = \frac{C_{\mathrm{ijkl}}(\mathbf{x})}{\Gamma(1-t)}\left(\frac{t}{t_0}\right)^{-2\gamma_{ijkl}} H(t), \tag{4}$$

where C_{ijkl} are the components of the real (elastic) stiffness tensor, and the anisotropic γ_{ijkl} can be calculated by $\gamma_{ijkl} = \arctan(1/Q_{ijkl})/\pi$. Using the property of the gamma function Γ (e.g., Caputo and Mainardi, 1971) and substituting equation 4 into equation 3 yield

$$\sigma_{ij}(\mathbf{x}, t) = C_{ijkl}(\mathbf{x}) \omega_0^{-2\gamma_{ijkl}} \partial_t^{2\gamma_{ijkl}} \varepsilon_{kl}(\mathbf{x}, t). \tag{5}$$

For the sake of simplicity, I drop the index $(\mathbf{x}, t)$ hereafter. Because of the symmetry in the stiffness tensor C_{ijkl} and anisotropic Q_{ijkl} tensor, the tensor becomes a symmetric stiffness matrix C_{ij} and anisotropic matrix Q_{ij}. I have defined the anisotropic Q_{ij} in the following section.

Anisotropic Q_{ij}

To consider the medium anelasticity, I adopt the following definition: Anisotropic Q_{ij} are the ratios of the real and imaginary parts of the corresponding stiffness coefficients (Carcione, 1992; Zhu and Tsvankin, 2006), $Q_{ij} = \mathrm{Re}(\tilde{C}_{ij})/\mathrm{Im}(\tilde{C}_{ij})$, where $\tilde{C}_{ij}$ are complex: $C_{ij} + iC_{ij}/Q_{ij}$. I assume that the symmetry of the quality factor $\mathbf{Q}$ in anisotropic media is the same as that of the stiffness $\mathbf{C}$. In TI media, the elastic model is fully characterized by five elastic parameters and density. Therefore, five additional anelastic parameters are needed to characterize such a TI attenuation behavior. In orthorhombic media, nine additional anelastic parameters are required to describe the viscoelastic behavior. The matrix Q_{ij} for a general anisotropic model (a triclinic medium) can be represented, using the compressed two-index Voigt notation, as follows:

$$Q_{ij} = \begin{pmatrix} Q_{11} & Q_{12} & Q_{13} & Q_{14} & Q_{15} & Q_{16} \\ Q_{12} & Q_{22} & Q_{23} & Q_{24} & Q_{25} & Q_{26} \\ Q_{13} & Q_{23} & Q_{33} & Q_{34} & Q_{35} & Q_{36} \\ Q_{14} & Q_{24} & Q_{34} & Q_{44} & Q_{45} & Q_{46} \\ Q_{15} & Q_{25} & Q_{35} & Q_{45} & Q_{55} & Q_{56} \\ Q_{16} & Q_{26} & Q_{36} & Q_{46} & Q_{56} & Q_{66} \end{pmatrix}. \tag{6}$$

Let us consider an isotropic Q_{ij}, in which the quality factor Q_{ij} is described by only two independent parameters, Q_{33} and Q_{55}, where $Q_{13} = Q_{12}$ is computed by $Q_{13} = Q_{33}C_{33} - 2(C_{55}/C_{33} - 2C_{55}Q_{33}/Q_{55})$ as defined in the paper by Zhu and Tsvankin (2006).

Therefore, in a general anisotropic medium, substituting the stiffness matrix 6 into equation 5 yields the constitutive equation of 3D viscoelastic-anisotropic media:

$$\begin{pmatrix}\sigma_{11}\\ \sigma_{22}\\ \sigma_{33}\\ \sigma_{23}\\ \sigma_{13}\\ \sigma_{12}\end{pmatrix} = \begin{pmatrix} D_{11} & D_{12} & D_{13} & D_{14} & D_{15} & D_{16}\\ D_{12} & D_{22} & D_{23} & D_{24} & D_{25} & D_{26}\\ D_{13} & D_{23} & D_{33} & D_{34} & D_{35} & D_{36}\\ D_{14} & D_{24} & D_{34} & D_{44} & D_{45} & D_{46}\\ D_{15} & D_{25} & D_{35} & D_{45} & D_{55} & D_{56}\\ D_{16} & D_{26} & D_{36} & D_{46} & D_{56} & D_{66}\end{pmatrix}\begin{pmatrix}\varepsilon_{11}\\ \varepsilon_{22}\\ \varepsilon_{33}\\ 2\varepsilon_{23}\\ 2\varepsilon_{13}\\ 2\varepsilon_{12}\end{pmatrix}, \tag{7}$$

where $D_{ij} = C_{ij}\omega_0^{-2\gamma_{ij}}\partial_t^{2\gamma_{ij}}$ and $\gamma_{ij} = \arctan(1/Q_{ij})/\pi$. Equation 7 plus the momentum conservation equations constitute the full viscoelastic anisotropic wave equation with anisotropic velocity and attenuation. It turns out that the resulting first-order system of anisotropic-viscoelastic wave equations has the same number of equations as the anisotropic elastic-wave equation.

Numerical methods

To solve the fractional time derivative, I use the GL approximation (Podlubny, 1999; Carcione et al., 2002) as follows:

$$\partial_t^{\gamma_{ij}}\varepsilon_{ij}(t) \approx \Delta t^{-\gamma_{ij}}\sum_{m=0}^{t/\Delta t}(-1)^m\binom{\gamma_{ij}}{m}\varepsilon_{ij}(t-m\Delta t). \tag{8}$$

The fractional derivative of wavefield variable $\varepsilon_{ij}(t)$ at time t depends on all the previous values of ε_{ij}. Recognizing that the fractional components of the binomial coefficient can be expressed as gamma functions G gives the following:

$$G_{ij}(m) = (-1)^m\binom{\gamma_{ij}}{m} = \frac{(-1)^m\Gamma(\gamma_{ij}+1)}{m!\Gamma(\gamma_{ij}+1-m)}. \tag{9}$$

Using the property of $\Gamma(\gamma_{ij}) = \Gamma(\gamma_{ij}+1)/\gamma_{ij}$; therefore, equation 9 can be reduced to a recursive relationship. When $m = 0$, equation 9 reduces to one. No parameters in equation 9 are spatially dependent. Therefore, in numerical implementation, equation 9 is precalculated before the time loop and is saved for later use.

This memory property of the fractional derivative requires the storage of past wavefields that increases the computational costs, especially saving 4D (x, y, z, t) field variables ε_{ij} in the 3D problem. The strategy of reducing the costs is to truncate the binomial coefficients for m exceeding an integer $N = t/\Delta t$ (total time step) (Podlubny, 1999). This allows truncation of the sum at $m = L$, $L \ll N$, where L is the effective memory length. In the implementation of the calculation of $\varepsilon_{ij}(t = n\Delta t)$, equation 8 becomes the following:

$$\partial_t^{\gamma_{ij}}\varepsilon_{ij}(n\Delta t) \approx \Delta t^{-\gamma_{ij}}\sum_{m=\max(0,n-L)}^{n}(-1)^m\binom{\gamma_{ij}}{m}\varepsilon_{ij}((n-m)\Delta t),$$
$$n <= N. \tag{10}$$

Wave equations for 2D TI media

I consider a TI medium model commonly used to describe shales or other layered rocks. Here, D_{ij} has five independent variables as five elastic stiffnesses C_{ij}, i.e., $D_{11}, D_{13}, D_{33}, D_{55}$, and D_{66}. For 2D modeling of P-SV waves in the x-z plane, the stress-strain relation is derived from equation 7 as follows:

$$\sigma_{11} = D_{11}\varepsilon_{11} + D_{13}\varepsilon_{33}, \tag{11a}$$

$$\sigma_{33} = D_{13}\varepsilon_{11} + D_{33}\varepsilon_{33}, \tag{11b}$$

$$\sigma_{13} = 2D_{55}\varepsilon_{13}. \tag{11c}$$

The law of conservation of momentum in 2D for the in-plane stresses is given as

$$\rho\partial_t^2 u_1 = \partial_1\sigma_{11} + \partial_3\sigma_{13}, \tag{12a}$$

$$\rho\partial_t^2 u_3 = \partial_1\sigma_{13} + \partial_3\sigma_{33}, \tag{12b}$$

where ρ is the material density and ∂_t^2 is the second-order time derivative. The strain components ε_{ij} can be obtained in terms of the displacement components as follows:

$$\varepsilon_{ij} = \frac{1}{2}(\partial_i u_j + \partial_j u_i). \tag{13}$$

The number of equations in the above system (equations 11a–11c, 12a, 12b, and 13) is the same as the anisotropic elastic-wave equation. If all anisotropic Q_{ij} values are infinity (thus $\gamma_{ij} = 0$), then the above system becomes the anisotropic elastic-wave equation, which can be solved using the open-source seismic modeling code *ewefd3d* in the Madagascar package (Fomel et al., 2013). In solving equation 12a and 12b, the second-order time derivatives are solved by standard second-order FD approximation. The first derivative ∂_j is approximated by a compact-centered FD with eighth-order accuracy (Weiss and Shragge, 2013). To eliminate the boundary reflections, four edges of the computational domain are treated as the mixed one-way and sponge-absorbing boundaries (Clayton and Enquist, 1977; Cerjan et al., 1985). Similar to FD elastic-anisotropic modeling steps in the *ewefd3d* code (Weiss and Shragge, 2013), the main steps in the FD viscoelastic-anisotropic modeling include the following:

1) precalculate gamma function $G_{ij}(m)$ according to equation 9
2) compute strains ε_{ij} from wavefield displacements according to equation 13
3) update current ε_{ij} from past ε_{ij} in a recursive manner in terms of equation 10, for example, $D_{11}\varepsilon_{11}(n\Delta t) = W\sum_{m=} max(0,n-L)^n G_{11}(m)\varepsilon_{11}((n-m)\Delta t), W = C_{11}\omega_0^{-2\gamma_{11}}\Delta t^{-\gamma_{11}}$
4) calculate stresses σ_{ij} from equation 11a to 11c
5) insert a stress source (if not an acceleration source)

6) compute acceleration from stress components (i.e., $\partial_j \sigma_{ij}$)
7) insert an acceleration source (if not a stress source)
8) compute the displacements from the displacement-stress relation (equation 12a and 12b)
9) apply the absorbing boundary conditions.

SYNTHETIC EXAMPLES

Verifying numerical solutions with theoretical Q values

To validate numerical solutions of the viscoelastic anisotropic wave equation, I generate the wavefields in a homogeneous viscoelastic VTI medium, estimate P- and SV-wave quality factors using the spectral-ratio method, and then, compare estimates with the theoretical Q-values calculated from equation A-3.

The size of the 2D homogeneous model is 2.56×2.56 km, and all their boundaries are absorbing. The model is discretized in a grid of 256×256. The spacings in the x- and z-directions are 10 m. Model parameters are $V_P = 6.0$ km/s, $V_S = 3.0$ km/s, $\rho = 2.0$ g/cm^3, $\varepsilon = 0.2$, and $\delta = 0.1$. I consider three Q_{ij} models: isotropic Q_{ij}, TI Q_{ij} I and II. All of the needed Q_{ij} properties are listed in Table 1. Note that only four are needed for the 2D modeling of the P- and SV-wave attenuations: Q_{11}, Q_{33}, Q_{13}, and Q_{55}. In VTI rock, the symmetry-axis-P-wave velocity (in the z-direction) is always less than the isotropy-plane (x-y) velocity, and therefore $C_{33} < C_{11}$. However, for the attenuation, there is an inverse relationship; i.e., the symmetry-axis attenuation $1/Q_{33}$ (in the z-direction) is greater than the horizontal attenuation $1/Q_{11}$ in the isotropy plane x-y (Carcione et al., 2012a). Thus, $Q_{33} < Q_{11}$.

Figure 1 shows the acquisition geometry in the form of circle with a radius of 1 km. The source of the vertical force (marked by star) was located in the center of the receivers' circle with 300 receivers set evenly around it. The source signal is in the form of Ricker wavelet with the dominant frequency of 30 Hz. The time step is 0.4 ms, and the recording time length of the wave simulation is 0.6 s. The memory length is set to the time length for the sake of high accuracy. The memory length is set equal to the total time length for the sake of high accuracy.

Figure 2 shows 2D simulations in four snapshots (Figure 2a–2d) of the vertical displacement component at time $t = 0.2$ s: without attenuation (Figure 2a), with isotropic attenuation (Figure 2b), with TI attenuation-I (Figure 2c), and with TI attenuation-II (Figure 2d). Figure 2e shows the difference between Figure 2b and 2c, and Figure 2f shows the difference between Figure 2b and 2d. All these cases clearly exhibit velocity anisotropy with the quasilongitudinal (qP) and quasitransversal (qSV) wavefronts. Amplitude with attenuation in Figure 2b–2d is weaker, as expected, than the case without attenuation (Figure 2a). The difference between snapshots with isotropic and anisotropic attenuation (Figure 2e and 2f) clearly

Table 1. Anisotropic Q_{ij} properties of three 2D homogeneous models.

Model	Q_{11}	Q_{13}	Q_{33}	Q_{55}
Isotropic attenuation	50	39	50	70
TI attenuation I	50	40	35	60
TI attenuation II	50	40	20	60

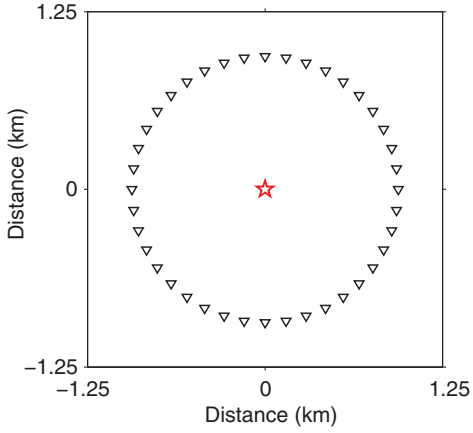

Figure 1. Source-receiver geometry of wave propagation simulation. The source is marked by red star, and the receivers are denoted by triangles. Every tenth receiver is shown for clarity.

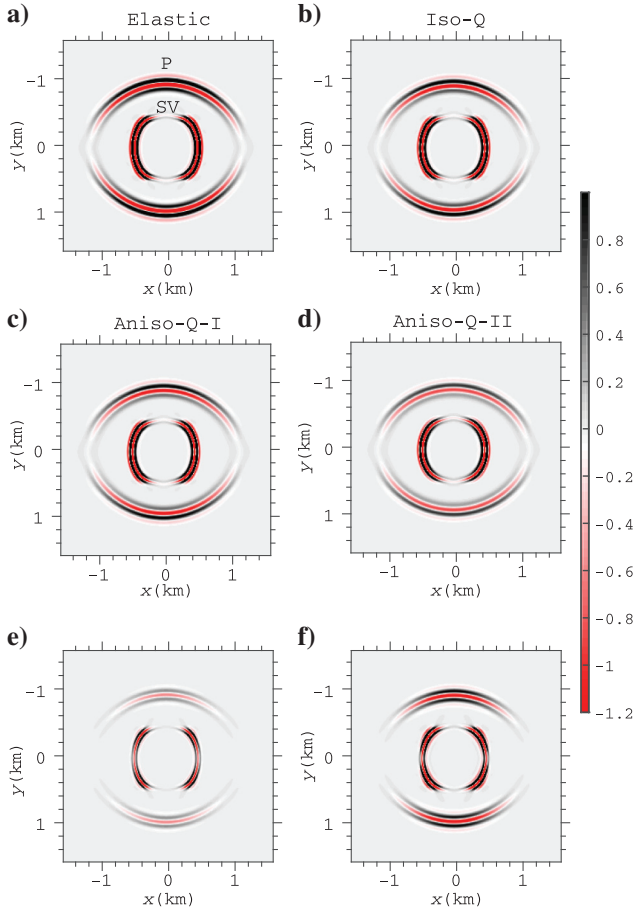

Figure 2. Snapshots (U_z displacement component) of anisotropy propagation of P-wave and SV-wave (a) without attenuation, (b) with isotropic attenuation, (c) with TI attenuation-I, and (d) with TI attenuation-II. Difference between (b) isotropic attenuation and (c) TI attenuation model-I is shown in (e). It is very clear that the anisotropic attenuation effects are direction dependent. Replacing $Q_{33} = 35$ by 20 in the TI attenuation model-I (other Q are fixed) leads to the more distinctive difference between (b) isotropic attenuation and (d) TI attenuation model-I as shown in (f).

manifests direction-dependent attenuation. Because the TI attenuation model and the isotropic attenuation model have the same $Q_P(0^\circ) = 50$, Figure 2e and 2f exhibits small difference of P-wave in 0° but a remarkable difference in 90°. Let us look at how $Q_{33} = 20$ makes a difference in two TI attenuation models. We can see a stronger difference in the P- and SV-waves in Figure 2f.

Figure 3 compares the vertical slice of four snapshots at the horizontal location of 0 m from Figure 2. There are (1) traces with attenuation that have delayed and reduced amplitude in comparison to the reference elastic (gray), (2) the trace with TI attenuation-I (blue) shows

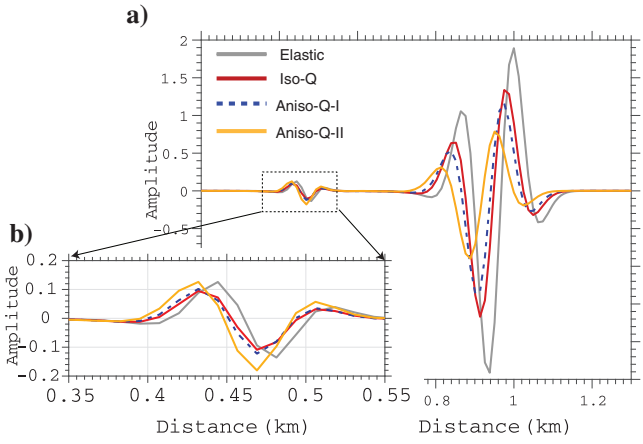

Figure 3. (a) A vertical slice of four snapshots through the center point $(0, 0)$ in Figure 2 for comparisons. (b) The magnified section for S-wave. In fact, because of the velocity dispersion, attenuation delays the phase (see colored traces) compared with the reference trace (gray). The phase and amplitude difference between isotropic and two TI attenuation cases is observable.

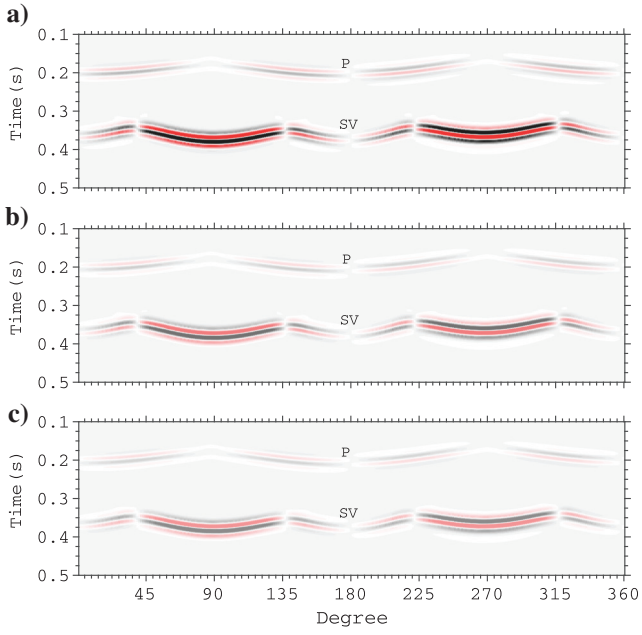

Figure 4. Simulated seismograms (U_z displacement component) of P- and SV-wave propagation in three models: (a) without attenuation, (b) with isotropic attenuation, and (c) with TI attenuation-I. The x-axis denotes phase angle θ, relatively symmetry axis of VTI medium.

small shifts and amplitude loss, (3) whereas the trace with TI attenuation-II (yellow) shows more shifts and amplitude loss. Therefore, the difference Q_{33}-s in these two TI attenuation models has a clear effect.

Figure 4 shows simulated full-recorded seismograms for the following three models: (Figure 4) without attenuation, (Figure 4b) with isotropic attenuation, and (Figure 4c) with TI attenuation. The model-input parameters are given in Table 1. All three models exhibit clear velocity anisotropy, with typical velocity-anisotropy patterns for qP- and qSV-waves. Compared with the model without attenuation (pure elastic anisotropy) as displayed in Figure 4a, both cases with attenuation (Figure 4b and 4c) exhibit a smaller amplitude and shifted phase. The isotropic attenuation (Figure 4b) and TI attenuation (Figure 4c) have their different impacts on the seismic amplitude. To study attenuation versus angle for these models in details, I estimate attenuation $(1/Q_{P,SV})$ using the spectral-ratio method for each trace, by comparing the spectra from the elastic model (Figure 3a) with the corresponding spectra from Figure 4b and 4c. The frequency range applied for this calculation by the spectral ratio method is 10–70 Hz. Figure 5 shows results of the attenuation estimation ($1/Q_P$ and $1/Q_{SV}$). Figure 5 compares estimated quality factors ($1/Q_P(\theta)$ and $1/Q_{SV}(\theta)$) (marked by the small circle points) with theoretical values (denoted by the solid line), where θ is the phase angle. Figure 5a and 5b shows estimations of P- and S-wave attenuation (marked by the small circle points) for the isotropic attenuation model. Estimations agree with the theoretical curve (solid line) very well. Figure 5c and 5d shows estimated P-wave attenuation $(1/Q_P)$ and SV-wave attenuation $(1/Q_{SV})$ (circles) for TI attenuation model I. Again,

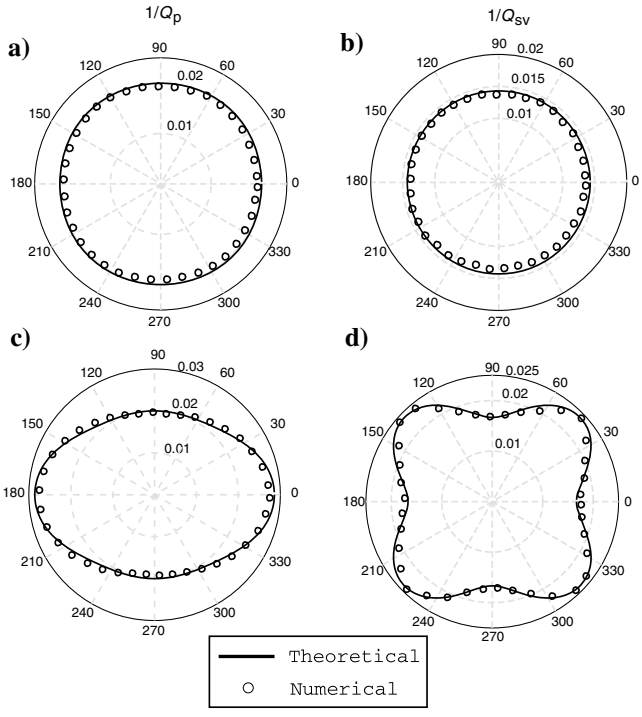

Figure 5. Model 1: Isotropic attenuation $1/Q_{P,SV}$ of (a) P-wave and (b) SV-wave as functions of the phase angle θ. Model 2: Anisotropic attenuation $1/Q_{P,SV}$ of (c) P-wave and (d) SV-wave as functions of the phase angle θ. Small circle points denote estimations of $1/Q_{P,SV}$ from comparisons of the waveforms in Figure 3 using the spectral ratio method (every fifth estimate is shown). The solid lines denote theoretical $1/Q_{P,SV}(\theta)$ values calculated from equation A-3.

the results of the estimation agree with the theoretical angle-dependent pattern (solid line).

2D TI layer-cake model

To show that it is able to handle a heterogeneous medium, I consider the case of a 2D model composed of four layers shown in Figure 6. The first and last layers are velocity isotropic and attenuation anisotropic. The second layer is composed of fine layers in which the sandstone-limestone-shale sequence was used to compute the anisotropic properties of layering, and the shale properties are taken from Thomsen (1986). The rocks' properties are listed in Table 2. The second layer is a VTI medium. The steps of computing fine-layering-induced anisotropy can be found in Carcione (1992). For the third layer, I consider a single set of vertical fractures embedded in an isotropic medium, resulting in horizontal TI. The properties of the isotropic medium are $V_P = 3.0$ km/s, $V_S = 2.0$ km/s, and $\rho = 2200$ kg/m^3. The following model-input parameters are used for the set of vertical fractures: the fracture stiffness $k_N = 9.0C_{11}$, $k_H = 8/3\,C_{66}$, $k_V = 4C_{55}$ and fracture viscosities $\eta_N = ak_N$, $\eta_H = ak_H$, and $\eta_V = ak_V$, where $a = 0.001$ s. Based on the fracture-induced anisotropy theory (Carcione et al., 2012b), the complex stiffness matrix components are computed. The resulting seismic viscoelastic-anisotropic properties are summarized in Table 3. The model has a size of 1000×1000 m. The model is discretized using grid spacing of 5 m. A force source is placed on the surface by adding the norm stresses σ_{11} and σ_{33} to equation 11a–11c. The source function is a Ricker wavelet with dominant frequency $f_0 = 30$ Hz, and the onset time $t_0 = 0.03$ s. The simulation uses 1700 time steps of 0.6 ms. A horizontal line of receivers is located 5 m below the source and is composed of 199 receivers. Absorbing conditions are used on the four edges of the grid to eliminate boundary reflections. The free-surface boundary is not considered. The memory length is the same as the time length (1700).

Figure 7 shows three snapshots at 0.15, 0.27, and 0.39 s of viscoelastic anisotropy (left) and elastic anisotropy (right). At 0.27 s,

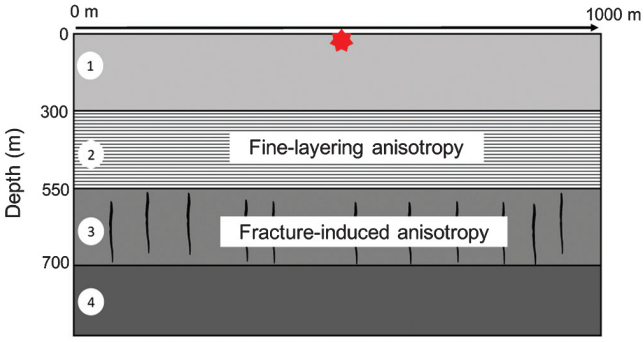

Figure 6. The 2D layered model. The second layer is composed of thin layers with the periodic sequence of limestone-sandstone-shale rocks denoted by thin lines. The third layer contains vertical fractures denoted by black polygons. The first and the last layers are velocity isotropic and attenuation anisotropic. The star denotes a source.

Table 2. Viscoelastic properties of three rock samples taken from Carcione (1992).

Rock type	Fraction	V_P(m/s)	V_S(m/s)	ρ (kg/m^3)	Q_P	Q_{SV}
Limestone	0.2	5443	3043	2700	80	40
Sandstone	0.3	2949	1615	2300	60	20
Shale	0.5	2074	869	2250	60	20

Table 3. Anisotropic-viscoelastic properties of 2D TI layered model. The other viscoelastic coefficients are zeros.

Layers	V_P (m/s)	V_S (m/s)	ρ (kg/m^3)	ε	δ	Q_{11}	Q_{13}	Q_{33}	Q_{55}
Layer 1	1900	1200	1800	0.0	0.0	30	11.6	30	50
Layer 2	2400	1100	2300	0.38	−0.08	85	240	79	40
Layer 3	3000	2000	2200	−0.16	−0.03	34	34	300	74
Layer 4	3200	1500	2500	0.0	0.0	60	46	60	100

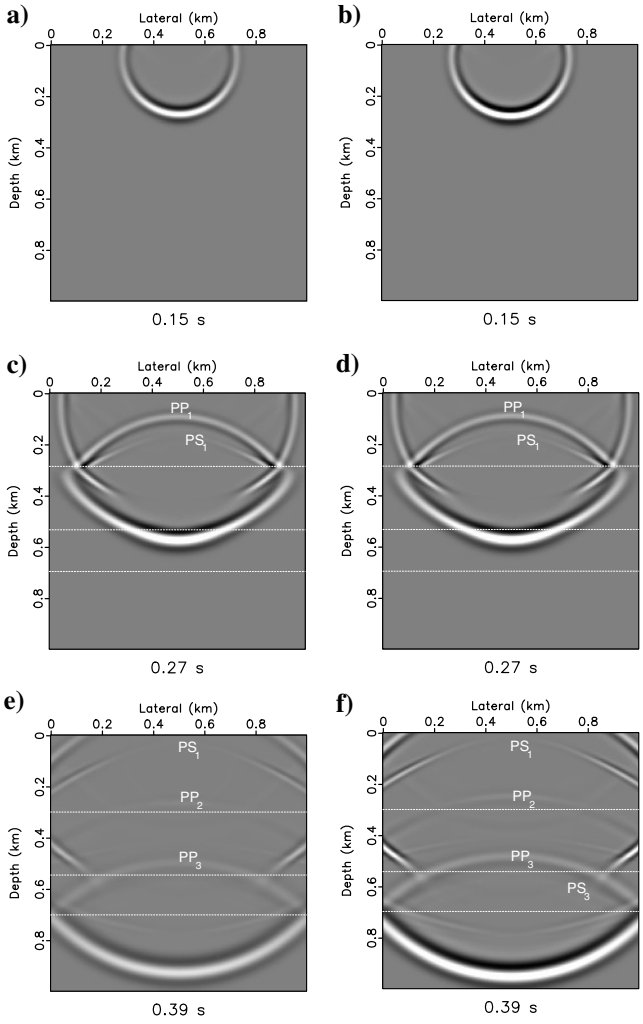

Figure 7. Snapshots (U_x-component) of anisotropy wave propagation with TI attenuation (a) 0.15, (c) 0.27, and (e) 0.39 s and without attenuation (b) 0.15, (d) 0.27, and (f) 0.39 s. The white lines denote the interface of different layers.

the attenuation effects on the PP transmission are clearly observed in the left panel. We can also see the weaker reflections (e.g., PP-reflection from the first interface, called PP_1) than the corresponding ones in the right panel. Similar observations are found at 0.39 s with complex reflections. Figure 8 compares two simulated seismograms for anisotropic wave propagation with TI attenuation (Figure 8a) and without attenuation (Figure 8b). The seismogram in Figure 8a clearly shows attenuated P-wave reflections (e.g., PP_1, PP_2, and PP_3) and converted waves (e.g., PS_1), where PP_i refers to P-wave reflections at the ith interface. Figure 8c displays comparison of two single traces at the 100th receiver selected from the seismograms in Figure 8a and 8b. One can see delayed reflections and reduced amplitudes because of the attenuation in the trace marked by the dashed line compared with the reference trace (marked by the solid line).

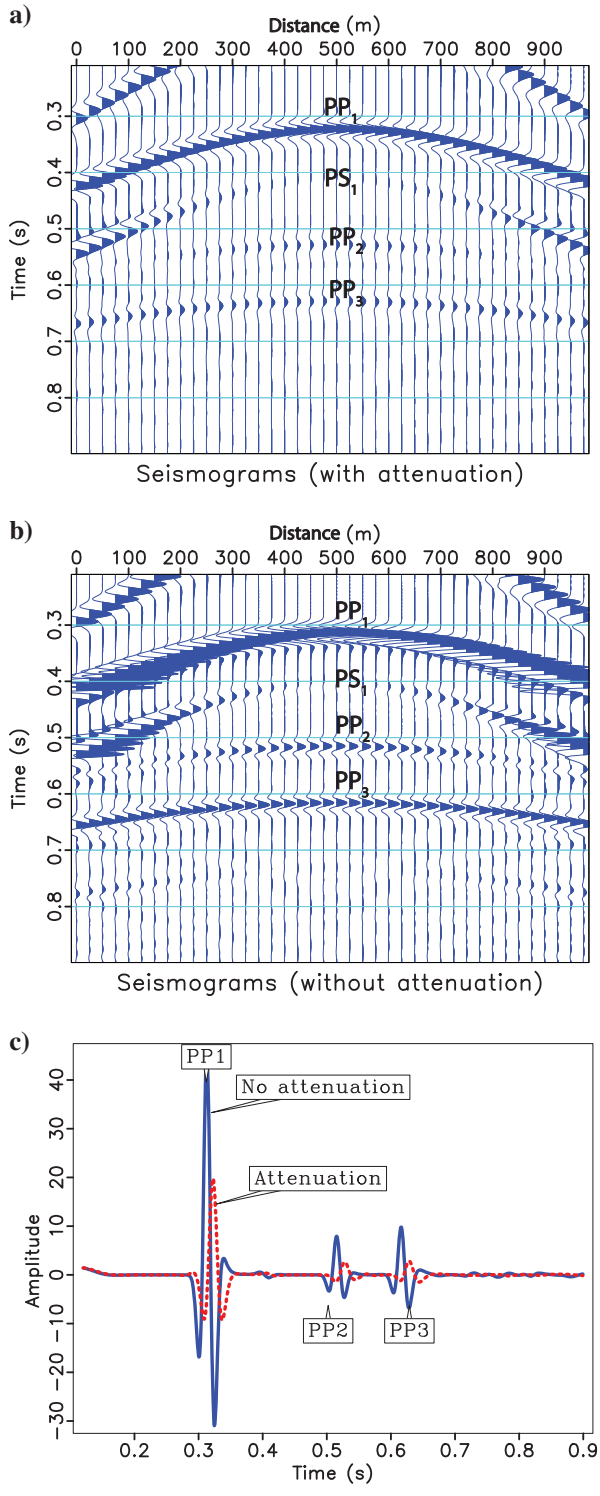

Figure 8. Synthetic seismograms (U_x displacement component) for anisotropic wave propagation with (a) TI attenuation and (b) without attenuation. (c) Two traces (magnified) from the previous seismograms (at the 100th receiver): comparing the cases of "no attenuation" (dashed line) and "attenuation" (solid line).

3D orthorhombic model

To show the generality of the method and to demonstrate its feasibility, I study the case of a 3D orthorhombic medium. Two orthogonal sets of fractures are embedded in the TI background medium. The following parameters are used for describing the TI background medium from Schoenberg and Helbig (1997): $C_{11} = 23$ GPa, $C_{13} = 5.75$ GPa, $C_{33} = 13.8$ GPa, $C_{55} = 4.6$ GPa, and $C_{66} = 6.9$ GPa. Following Carcione et al. (2012b), I set two sets of fractures in the model (one is for vertical fractures at 0° and the other for horizontal fractures at 90°) with the same fracture stiffness for the 90° fracture as in the previous example: $k_N = 9.0C_{11}$, $k_H = 8/3\,C_{66}$, and $k_V = 4C_{55}$. For the 0° fractures, I use half of the stiffness of the 90° fractures. Fracture viscosities for both fracture sets are $\eta_N = ak_N$, $\eta_H = ak_H$, and $\eta_V = ak_V$, where $a = 0.001$ s. The complex stiffness matrix is obtained using Carcione et al. (2012b)'s equation 19 as follows:

Table 4. The Orthorhombic Q_{ij} properties.

Q_{11}	Q_{12}	Q_{13}	Q_{22}	Q_{23}	Q_{33}	Q_{44}	Q_{55}	Q_{66}
28.8	12.4	21.6	17.9	16	146	10.2	17.2	6.3

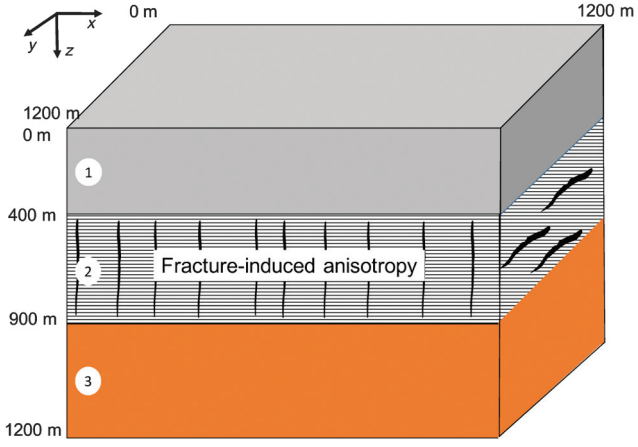

Figure 9. A 3D layered model. The middle layer contains two orthogonal fracture sets that induce orthorhombic anisotropy of velocity and attenuation.

$$\tilde{C}_{ij}=\begin{pmatrix} 20.34+0.70i & 6.93+0.56i & 4.87+0.22i & 0 & 0 & 0 \\ 6.93+0.56i & 18.83+1.05i & 4.6+0.29i & 0 & 0 & 0 \\ 4.87+0.22i & 4.6+0.29i & 13.44+0.09i & 0 & 0 & 0 \\ 0 & 0 & 0 & 3.13+0.31i & 0 & 0 \\ 0 & 0 & 0 & 0 & 3.73+0.22i & 0 \\ 0 & 0 & 0 & 0 & 0 & 3.32+0.53i \end{pmatrix}, \tag{14}$$

in GPa, where i is the imaginary unit. There are nine components of the quality factor matrix $\mathbf{Q}$ derived as shown in Table 4.

Let us consider an example of a three-layered medium shown in Figure 9. The top layer is isotropic. It has $C_{11} = 18$ GPa, $C_{13} = 9$ GPa, and $C_{55} = 4.5$ GPa; and isotropic quality factors $Q_{33} = 30$ and $Q_{55} = 20$, and density $\rho = 2.0$ g/cm^3. The middle layer is the fractured medium represented by the orthorbombic model for the velocity and attenuation; its properties are given in equation 14 and Table 4. The bottom shale layer is described by the VTI model, with the following parameters taken from Jones and Wang (1981) for the Greenhorn shale: $C_{11} = 14.47$ GPa, $C_{12} = 4.51$GPa, $C_{13} = 9.57$ GPa, $C_{55} = 2.28$ GPa, $C_{66} = 3$ GPa, and the homogeneous quality factor is $Q = 100$. The density is $\rho = 2.59$ g/cm^3.

The model dimension is $1200 \times 1200 \times 1200$ m. There is an explosive source placed inside the block at the depth of 50 m, simulated by adding the equal force to normal stresses σ_{11}, σ_{22}, and σ_{33}. The Ricker wavelet is used for the wave source, with the dominant frequency $f_0 = 25$ Hz, and the time onset $t_0 = 0.04$ s. Receivers are placed in every grid point in the x-y plane at the depth of 20 m. The medium is discretized using a grid of $120 \times 120 \times 120$. The length of simulation is propagated for 1 s using a time step of 0.001 s for a total of 1000 time steps. The memory length is 500. In the modeling, absorbing boundaries are applied at all four edges.

Figure 10 shows synthetic seismograms (three displacement components recorded in the receiver points), corresponding to the attenuation case and nonattenuation case. As expected, because of attenuation, the weaker reflections are in the attenuation case (Figure 10b, 10d, and 10f), in particular, the first and second layers, than in the nonattenuation case (Figure 10a, 10c, and 10e).

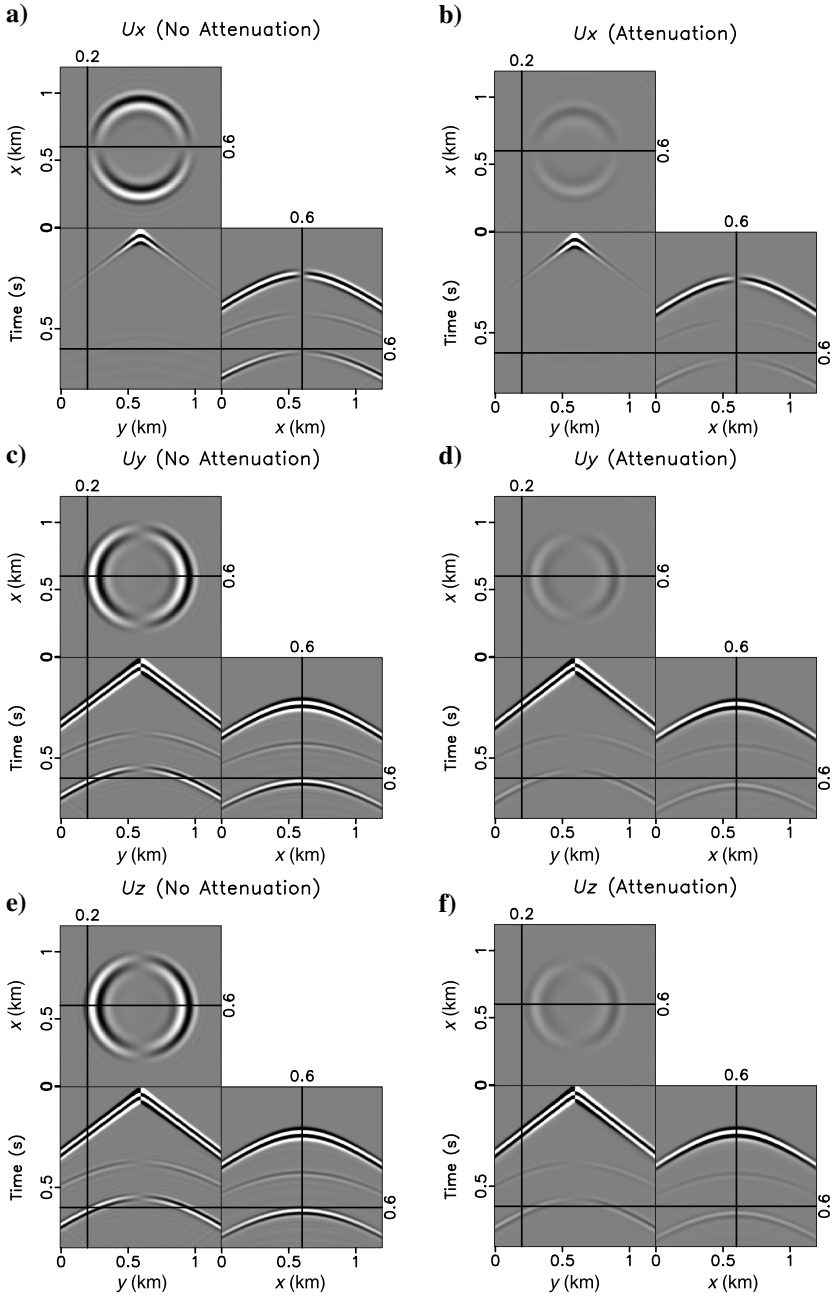

Figure 10. Snapshots (U_x-, U_y-, and U_z-displacement components) for wave propagation in 3D orthorhombic model (shown in Figure 9) (a, c, and e) without attenuation and (b, d, and f) with attenuation. All figure parts are scaled in the same range.

DISCUSSION

Solving the fractional time derivative of a variable $\varepsilon(\mathbf{x}, t)$ (where $\mathbf{x}$ is the spatial coordinate) has to demand huge computational memory caused by the effect of nonlocal derivatives in time in which all previous time points contribute to the current iteration. For instance, the 3D orthorhombic example (the model size is $120 \times 120 \times 120$) needs approximately 90 GB computer memory to save all temporary wavefields. It is prohibitive to store all the past history of wavefields in a realistic 3D dimension problem, which is a big challenge to use for a seismic inverse problem. Using the truncation principle (Podlubny, 1999) can reduce the computational memory a bit, but it is the tradeoff between the memory and numerical errors. Carcione et al. (2002) reformulate the wave equation by adding the fractional order by one. He shows that this reformulation can reduce the memory storage by one order but achieve the same accuracy. The same idea was used for accel-

erating the solving of the viscoelastic case (Carcione, 2009) and the Kevin-Voigt relation for medical dissipation media (Caputo et al., 2011). MacDonald et al. (2015) introduce an adaptive time-step memory-storage strategy to compute temporally weighted history that includes contributions from the entire past history. By maintaining the same or higher accuracy, fewer past wavefield actually are stored, thereby greatly improving computational efficiency. It is not clear whether or not it needs the same order of computational memory as the truncation method. This strategy apparently still faces the memory problem. Instead of using fractional time derivatives, Chen and Holm (2004) suggest using fractional spatial derivatives to completely avoid the memory storage (Carcione, 2010). Zhu and Harris (2014) develop a viscoacoustic wave equation for seismic modeling and demonstrate that the new fractional Laplacian formulation can approximate the frequency-independent Q model very well. This strategy has been implemented in solving viscoelastic wave equations (Zhu and Carcione, 2014) and was further used for (least-squares) reverse-time imaging problems (Zhu, 2014; Zhu et al., 2014; Sun et al., 2016; Zhu and Sun, 2017) and full-waveform inversion (Xue et al., 2016).

It is worthwhile to note that acoustic approximation to the elastic anisotropy wave equation (e.g., acoustic TI) holds for the wavefield phase but not for the amplitude, which is originally pointed out by Alkhalifah (2000). Analogously, if we simplify the formulation of viscoelastic-anisotropic wave equation to the viscoacoustic-anisotropic case, the amplitude loss appears to be incorrect.

CONCLUSION

I present a viscoelastic anisotropic wave equation with the representation of arbitrary velocity and attenuation anisotropy. Attenuation anisotropy is expressed in terms of fractional time derivatives in the wave equation based on the frequency-independent Q model. To circumvent the storage of the past history of wavefields to compute the current wavefield in the limited memory, the truncated GL is used to solve the fractional time derivative operator. The derived wave equation is found to provide well approximations of anisotropic attenuation by comparing with the theoretical attenuation solutions in a 2D homogeneous TI Q medium. Simulated results show that anisotropic attenuation effects are significantly different from isotropic attenuation effects in the seismograms. The formulation can be used to handle heterogeneous anisotropic Q models and deal with fully anisotropic 3D models, by studying an orthorhombic 3D medium. For practical 3D modeling, the drawback of the GL scheme is the high demand of computer memory. Searching for a method to reduce this need of computational memory will be necessary in further practice.

ACKNOWLEDGMENTS

I thank V. Grechka, T. Chichinina, and two anonymous reviewers for their constructive and insightful comments that helped to significantly improve the quality of this paper. The study was supported by the start-up funding from the Department of Geosciences at the Pennsylvania State University and Distinguished Postdoctoral Fellowship in the Jackson School of Geosciences at the University of Texas at Austin.

APPENDIX A

PLANE-WAVE SOLUTION FOR A TI MEDIUM

Let us consider wave propagation in a plane containing the symmetry axis (z-axis) of a TI medium. Using the general plane-wave solution yields to the corresponding complex velocities (Carcione, 2014) gives the following derivation:

$$v_1 = \sqrt{\rho^{-1}(\tilde{C}_{66}l_1^2 + \tilde{C}_{55}l_2^2)}, \tag{A-1a}$$

$$v_2 = \sqrt{(2\rho)^{-1}(\tilde{C}_{11}l_1^2 + \tilde{C}_{33}l_3^2 + \tilde{C}_{55} - A)}, \tag{A-1b}$$

$$v_3 = \sqrt{(2\rho)^{-1}(\tilde{C}_{11}l_1^2 + \tilde{C}_{33}l_3^2 + \tilde{C}_{55} + A)}, \tag{A-1c}$$

$$A = \sqrt{[(\tilde{C}_{11} - \tilde{C}_{55})l_1^2 + (\tilde{C}_{55} - \tilde{C}_{33})l_3^2]^2 + 4[(\tilde{C}_{13} + p_{55})l_1 l_3]^2}, \tag{A-1d}$$

where the subscript 1 denotes the pure mode (the SH-wave), and the subscripts 2 and 3 are the qS- and qP-waves, respectively, and l_1, l_2, l_3 are the direction vectors of phase slowness. The phase velocity v^{ph} is given by

$$v_i^{\text{ph}} = \left[\text{Re}\left(\frac{1}{v_i}\right)\right]^{-1}, \tag{A-2}$$

and the quality factor is given as

$$Q_i = \frac{\text{Re}(v_i^2)}{\text{Im}(v_i^2)}, \quad i = 1, 2, 3. \tag{A-3}$$

REFERENCES

Alkhalifah, T., 2000, An acoustic wave equation for anisotropic media: Geophysics, **65**, 1239–1250, doi: 10.1190/1.1444815.

Anderson, D. L., 1989, Theory of the earth: Blackwell Scientific Publications.

Arts, R. J., and P. N. J. Rasolofosaon, 1992, Approximation of velocity and attenuation in general anisotropic rocks: 62nd Annual International Meeting, SEG, Expanded Abstracts, 640–643.

Bai, T., and I. Tsvankin, 2016, Time-domain finite-difference modeling for attenuative anisotropic media: Geophysics, **81**, no. 2, C69–C77, doi: 10.1190/geo2015-0424.1.

Best, A. I., J. Sothcott, and C. McCann, 2007, A laboratory study of seismic velocity and attenuation anisotropy in near-surface sedimentary rocks: Geophysical Prospecting, **55**, 609–625, doi: 10.1111/j.1365-2478.2007.00642.x.

Caputo, M., J. M. Carcione, and F. Cavallini, 2011, Wave simulation in biologic media based on the kelvin-voigt fractional-derivative stress-strain relation: Ultrasound in Medicine and Biology, **37**, 996–1004, doi: 10.1016/j.ultrasmedbio.2011.03.009.

Caputo, M., and F. Mainardi, 1971, A new dissipation model based on memory mechanism: Pure and Applied Geophysics, **91**, 134–147, doi: 10.1007/BF00879562.

Carcione, J. M., 1992, Anisotropic Q and velocity dispersion of finely layered media1: Geophysical Prospecting, **40**, 761–783, doi: 10.1111/j.1365-2478.1992.tb00551.x.

Carcione, J. M., 2009, Theory and modeling of constant-Q P- and S-waves using fractional time derivatives: Geophysics, **74**, no. 1, T1–T11, doi: 10.1190/1.3008548.

Carcione, J. M., 2010, A generalization of the Fourier pseudospectral method: Geophysics, **75**, no. 6, A53–A56, doi: 10.1190/1.3509472.
Carcione, J. M., 2014, Wave fields in real media: Theory and numerical simulation of wave propagation in anisotropic, anelastic, porous and electromagnetic media (3rd ed.): Elsevier.
Carcione, J. M., F. Cavallini, F. Mainardi, and A. Hanyga, 2002, Time-domain seismic modeling of constant-Q wave propagation using fractional derivatives: Pure and Applied Geophysics, **159**, 1719–1736, doi: 10.1007/s00024-002-8705-z.
Carcione, J. M., S. Picotti, and J. E. Santos, 2012a, Numerical experiments of fracture-induced velocity and attenuation anisotropy: Geophysical Journal International, **191**, 1179–1191.
Carcione, J. M., J. E. Santos, and S. Picotti, 2012b, Fracture-induced anisotropic attenuation: Rock Mechanics and Rock Engineering, **45**, 929–942, doi: 10.1007/s00603-012-0237-y.
Cerjan, C., C. Kosloff, R. Kosloff, and M. Reshef, 1985, A non-reflecting boundary condition for discrete acoustic and elastic wave equation: Geophysics, **50**, 705–708, doi: 10.1190/1.1441945.
Chen, W., and S. Holm, 2004, Fractional Laplacian time-space models for linear and nonlinear lossy media exhibiting arbitrary frequency power-law dependency: The Journal of the Acoustical Society of America, **115**, 1424–1430, doi: 10.1121/1.1646399.
Chichinina, T., I. Obolentseva, L. Gik, B. Bobrov, and G. Ronquillo-Jarillo, 2009, Attenuation anisotropy in the linear-slip model: Interpretation of physical modeling data: Geophysics, **74**, no. 5, WB165–WB176, doi: 10.1190/1.3173806.
Clayton, R., and B. Enquist, 1977, Absorbing boundary conditions for acoustic and elastic wave equations: Bulletin of the Seismological Society of America, **67**, 1529–1540.
Domnesteanu, P., C. McCann, and J. Sothcott, 2002, Velocity anisotropy and attenuation of shale in under- and overpressured conditions: Geophysical Prospecting, **50**, 487–503, doi: 10.1046/j.1365-2478.2002.00329.x.
Fomel, S., P. Sava, I. Vlad, Y. Liu, and V. Bashkardin, 2013, Madagascar: Open-source software project for multidimensional data analysis and reproducible computational experiments: Journal of Open Research Software, **1**, e8, doi: 10.5334/jors.ag.
Helbig, K., 1994, Foundations of anisotropy for exploration seismic: Section I. Seismic exploration: Pergamon Press.
Hosten, B., M. Deschamps, and B. Tittmann, 1987, Inhomogeneous wave generation and propagation in lossy anisotropic solids: Application to the characterization of viscoelastic composite materials: Journal of the Acoustical Society of America, **82**, 1763–1770.
Jones, L. E. A., and H. F. Wang, 1981, Ultrasonic velocities in cretaceous shales from the Williston basin: Geophysics, **46**, 288–297, doi: 10.1190/1.1441199.
Kjartansson, E., 1979, Constant-Q wave propagation and attenuation: Journal of Geophysical Research, **84**, 4737–4748, doi: 10.1029/JB084iB09p04737.
Komatitsch, D., and J. Tromp, 1999, Introduction to the spectral element method for three dimensional seismic wave propagation: Geophysical Journal International, **139**, 806–822, doi: 10.1046/j.1365-246x.1999.00967.x.
Liu, E., S. Crampin, J. H. Queen, and W. D. Rizer, 1993, Velocity and attenuation anisotropy caused by microcracks and microfractures in a multiazimuth reverse VSP: Canadian Journal of Exploration Geophysics, **29**, 177–188.
Liu, H. P., D. L. Anderson, and H. Kanamori, 1976, Velocity dispersion due to anelasticity: Implication for seismology and mantle composition: Geophysical Journal of the Royal Astronomical Society, **47**, 41–58, doi: 10.1111/j.1365-246X.1976.tb01261.x.
Lynn, H. B., D. Campagna, K. M. Simon, and W. E. Beckham, 1999, Relationship of P-wave seismic attributes, azimuthal anisotropy, and commercial gas pay in 3-d P-wave multiazimuth data, Rulison field, Piceance basin, Colorado: Geophysics, **64**, 1293–1311, doi: 10.1190/1.1444635.
MacDonald, C. L., N. Bhattacharya, B. P. Sprouse, and G. A. Silva, 2015, Efficient computation of the Grünwald–Letnikov fractional diffusion derivative using adaptive time step memory: Journal of Computational Physics, **297**, 221–236, doi: 10.1016/j.jcp.2015.04.048.
Podlubny, I., 1999, Fractional differential equations: Academic Press.
Schoenberg, M., and K. Helbig, 1997, Orthorhombic media: Modeling elastic wave behavior in a vertically fractured earth: Geophysics, **62**, 1954–1974, doi: 10.1190/1.1444297.
Shi, G., and J. Deng, 2005, The attenuation anisotropy of mudstones and shales in subsurface formations: Science China (Earth Science), **48**, 1882–1890, doi: 10.1360/03yd0426.
Sun, J., S. Fomel, T. Zhu, and J. Hu, 2016, Q-compensated least-squares reverse time migration using low-rank one-step wave extrapolation: Geophysics, **81**, no. 4, S271–S279, doi: 10.1190/geo2015-0520.1.
Tao, G., and M. S. King, 1990, Shear-wave velocity and Q anisotropy in rocks: A laboratory study: International Journal of Rock Mechanics and Mining Sciences and Geomechanics Abstracts, **27**, 353–361, doi: 10.1016/0148-9062(90)92710-V.
Thomsen, L., 1986, Weak elastic anisotropy: Geophysics, **51**, 1954–1966, doi: 10.1190/1.1442051.
Thomsen, L., 2014, Understanding seismic anisotropy in exploration and exploitation (2nd ed.): SEG.
Tsvankin, I., 2012, Seismic signatures and analysis of reflection data in anisotropic media (3rd ed.): SEG.
Weiss, R. M., and J. Shragge, 2013, Solving 3d anisotropic elastic wave equations on parallel GPU devices: Geophysics, **78**, no. 2, F7–F15, doi: 10.1190/geo2012-0063.1.
Xue, Z., J. Sun, S. Fomel, and T. Zhu, 2016, Q-compensated full-waveform inversion using constant-Q wave equation: 86th Annual International Meeting, SEG, Expanded Abstracts, 1063–1068.
Zhu, T., 2014, Time-reverse modelling of acoustic wave propagation in attenuating media: Geophysical Journal International, **197**, 483–494, doi: 10.1093/gji/ggt519.
Zhu, T., and J. M. Carcione, 2014, Theory and modelling of constant-Q P- and S-waves using fractional spatial derivatives: Geophysical Journal International, **196**, 1787–1795, doi: 10.1093/gji/ggt483.
Zhu, T., J. M. Carcione, and J. M. Harris, 2013, Approximating constant-Q seismic propagation in the time domain: Geophysical Prospecting, **61**, 931–940, doi: 10.1111/1365-2478.12044.
Zhu, T., and J. M. Harris, 2014, Modeling acoustic wave propagation in heterogeneous attenuating media using decoupled fractional Laplacians: Geophysics, **79**, no. 3, T105–T116, doi: 10.1190/geo2013-0245.1.
Zhu, T., J. M. Harris, and B. Biondi, 2014, Q-compensated reverse-time migration: Geophysics, **79**, no. 3, S77–S87, doi: 10.1190/geo2013-0344.1.
Zhu, T., and J. Sun, 2017, Viscoelastic reverse time migration with attenuation compensation: Geophysics, **82**, no. 2, S61–S73, doi: 10.1190/geo2016-0239.1.
Zhu, Y., and I. Tsvankin, 2006, Plane-wave propagation in attenuative transversely isotropic media: Geophysics, **71**, no. 2, T17–T30, doi: 10.1190/1.2187792.
Zhu, Y., I. Tsvankin, P. Dewangan, and K. V. Wijk, 2007a, Physical modeling and analysis of P-wave attenuation anisotropy in transversely isotropic media: Geophysics, **72**, no. 1, D1–D7, doi: 10.1190/1.2374797.
Zhu, Y., I. Tsvankin, and I. Vasconcelos, 2007b, Effective attenuation anisotropy of thin-layered media: Geophysics, **72**, no. 5, D93–D106, doi: 10.1190/1.2754185.
Zhubayev, A., M. E. Houben, D. M. J. Smeulders, and A. Barnhoorn, 2016, Ultrasonic velocity and attenuation anisotropy of shales, Whitby, United Kingdom: Geophysics, **81**, no. 1, D45–D56, doi: 10.1190/geo2015-0211.1.